Supplementary Materials for

Extreme Optical Nonlinearity (> 500) at Room Temperature through Sublattice Reconstruction

This file includes:

Materials and Methods

Materials

Oleic acid (90 %), 1-octadecene (90%), lutetium(III) chloride hexahydrate ($LuCl_3 \cdot 6H_2O$, 99.9%, Aladdin), yttrium(III) chloride hexahydrate ($YCl_3 \cdot 6H_2O$, 99.9%), thulium(III) chloride hexahydrate ($TmCl_3 \cdot 6H_2O$, 99.9%), yttrium oxide (Y_2O_3; 99.99%), gadolinium (Gd_2O_3; 99.99%), trifluoroacetic acid (TFA; 99.9%), sodium trifluoroacetate (CF_3COONa, 98%), sodium hydroxide (NaOH; 98%), ammonium fluoride (NH_4F; 98%), ethylene glycol (EG; 99.8%) and nitrosonium tetrafluoroborate ($NOBF_4$; 95%) were purchased from Sigma–Aldrich, unless otherwise noted and all were used as received without further purification.

Synthesis of ~27 nm NaY/LuF_4:Tm nanocrystals

Nanocrystals were synthesized using a modified version of previously reported protocols[1,2]. In a typical experiment, 1 mmol of $LuCl_3 \cdot 6H_2O$, $YCl_3 \cdot 6H_2O$, and $TmCl_3 \cdot 6H_2O$ in various molar ratios were introduced along with 10.0 mL of oleic acid and 15.0 mL of 1-octadecene. The mixture was heated to 130 °C and kept under vacuum for 60 min to facilitate the formation of lanthanide-oleate complexes. Subsequently, 0.10 g of NaOH was introduced at 130 °C for 60 min until dissolved, followed by adding 0.148 g of NH_4F with continuous stirring for an additional 60 min. The mixture was then vacuumed for 20 min to remove volatile residues. The remaining mixture was heated to 310 °C and maintained at this temperature for 90 min under an inert nitrogen environment. After cooling to room temperature, the resulting nanocrystals were collected by centrifugation, washed three times with ethanol, and dispersed in 10.0 mL of cyclohexane for further use.

Synthesis of 18 nm $NaLuF_4$:Tm(15%) nanocrystals

For the synthesis of small nanocrystals, 1 mmol $LuCl_3 \cdot 6H_2O$ and $TmCl_3 \cdot 6H_2O$ in the designed molar ratios were added along with 10.0 mL of oleic acid and 15.0 mL of 1-octadecene. The mixture was heated to 130 °C and kept for 60 min under vacuum to facilitate the formation of lanthanide-oleate complexes. Subsequently, 0.15 g of NaOH was introduced at 130 °C for 60 min until dissolved, followed by adding 0.225 g of NH_4F with continuous stirring for an additional 60 min. The mixture was then vacuumed for 20 minutes to remove volatile residues. The remaining mixture was heated to 305 °C and maintained at this temperature for 60 min under an inert nitrogen environment. After cooling to room temperature, the resulting nanocrystals were collected by centrifugation, washed

three times with ethanol, and dispersed in 10.0 mL of cyclohexane for further use.

Synthesis of 176 nm $NaLuF_4$:Tm(15%) nanocrystals

For the synthesis of large-sized nanocrystals, 2 mmol of $LuCl_3 \cdot 6H_2O$ and $TmCl_3 \cdot 6H_2O$ in the intended ratio were added together with 15.0 mL of oleic acid and 35.0 mL of 1-octadecene. The mixture was heated to 130 °C and maintained at this temperature for 60 min to facilitate the formation of lanthanide-oleate complexes. Subsequently, the solution was cooled to 50 °C and a 10 mL methanol solution containing NH_4F (0.296 g) and NaOH (0.2 g) was introduced. After stirring for one hour, the solution was heated to 110 °C and the remaining volatile impurities were removed under vacuum. The remaining mixture was then heated to 310 °C and held at this temperature for 90 min under an inert nitrogen environment. After cooling to room temperature, the resulting nanocrystals were collected by centrifugation, washed three times with ethanol, and dispersed in 10.0 mL of cyclohexane for further use.

Synthesis of $NaYF_4$:Tm(15%)@$NaY_{80}/Gd_{20}F_4$

Core-shell nanocrystals were obtained via thermal decomposition. $Y(CF_3COO)_3$ and $Gd(CF_3COO)_3$ were collected by adding excess TFA to the corresponding oxide. In a typical procedure, 0.07 g of CF_3COONa, 0.14 g of $Y(CF_3COO)_3$, and 0.04 g of $Gd(CF_3COO)_3$ as shell precursors were added to a 50-mL flask containing 0.4 mmol of core cyclohexane solution, 6.0 mL of oleic acid and 6.0 mL of 1-octadecene. The mixture was then heated to 110 °C and kept under vacuum for 20 min to remove the volatile residue. The remaining mixture was heated to 300 °C and maintained at this temperature for 45 min under an inert nitrogen environment. After cooling to room temperature, the resulting nanocrystals were collected by centrifugation, washed three times with ethanol, and dispersed in 4.0 mL of cyclohexane for further use.

Preparation of ligand-free nanocrystals

Oleic acid ligands bound to nanocrystal surfaces were removed by using $NOBF_4$. In a typical procedure, a solution of nanoparticles dispersed in cyclohexane (1 mL) was combined with an *N*,*N*-dimethylformamide (DMF) solution of $NOBF_4$ (40 mg/mL, 1 mL). The resulting mixture was sonicated for two minutes, facilitating the extraction of nanoparticles from the upper cyclohexane layer to the underlying DMF layer. After removal of the upper cyclohexane layer, the nanoparticles dispersed in the underlying DMF layer were precipitated by adding 4.0 mL of ethanol and subsequently

centrifuged at 15000 rpm for 5 minutes. Finally, the ligand-free nanocrystals were dispersed in either 1.0 mL of ethanol or water for subsequent use.

Self-assembly of monolayer 176 nm $NaLuF_4$:Tm(15%) nanocrystals

Self-assembly of the nanocrystals was performed using a modified version of the previously reported interfacial assembly method[3]. In a typical experiment, 10 μL of a 0.1 mM core cyclohexane solution was drop-cast onto the ethylene glycol surface in a half-filled Teflon well of 3 × 3 × 2 cm^3. To slow the evaporation of the solvent, the well was covered with a glass slide. After 30 min, the nanocrystal film was transferred to glass substrates and further dried in a vacuum chamber at 50 °C overnight to remove excess ethylene glycol for subsequent use.

Characterization

The size and morphology of nanocrystals were characterized using a transmission electron microscope (JEOL 2010F) operated at an acceleration voltage of 200 kV. The thickness of the spin-coated films was measured using a KLA Tencor P16 stylus profiler. X-ray photoelectron spectra (XPS) were acquired at room temperature using a Kratos Amicus ESCA 3400. Room-temperature photoluminescence spectra and dynamics were recorded at room temperature using an FLS1000 from Edinburgh Instruments. Correlative imaging was performed using a JEOL JSM-6701F field-emission scanning electron microscope (FESEM) with a labeled pattern for navigation. Powder X-ray diffraction (XRD) patterns were recorded with a Bruker D8 diffractometer using Cu/Ka radiation (l=1.5406 Å). Absorption spectra of the solid samples were measured using a Shimadzu UV-2600 spectrometer equipped with an integrating sphere. Raman spectra were measured using a Renishaw invia Raman system, utilizing a 532-nm laser and 1800 l/mm gratings. Elemental composition analysis was performed with an inductively coupled plasma optical emission spectrometer (ICP-OES), specifically the Perkin Elmer Avio 500 model. High-angle annular dark-field (HAADF) images were recorded with an aberration-corrected JEOL ARM200F scanning transmission electron microscopy equipped with a cold field-emission gun and operated at 200 kV. X-ray energy dispersive spectroscopy (EDS) analysis was conducted on the JEOL ARM200F using an Oxford Instrument spectrometer. Tm-L_3 edge EXAFS measurements were operated at the XAFCA beamline of the Singapore Synchrotron Light Source at 0.7 GeV and a current of 150 mA, using a monochromator equipped with two Si (111) crystals in focusing mode. Samples were analyzed in transmission mode at room temperature, with data analysis performed using Athena and Artemis[4-6].

Optical characterization of photon-avalanching nanoparticles

Single-particle imaging**:** To prepare for imaging, 100 µl of a 50 nM nanoparticle suspension in cyclohexane were spin-coated onto a clean coverslip at 1500 rpm for 30 seconds. A 1064-nm continuous-wave diode laser (MDL-S-1064-SM) illuminated the sample through the back aperture of a 100× immersion-oil objective with a numerical aperture (NA) of 1.45 (Nikon, UPLAN CFI Plan Apochromat Lambda D 100X Oil). The sample was positioned on a three-dimensional (XYZ) piezo stage (Physik Instrumente, P-561.3CD) for precise focusing.

Film sample measurements**:** For these experiments, 100 µl of a 0.1 mM nanoparticle suspension in cyclohexane was spin-coated on a clean coverslip at 1500 rpm for 30 seconds. An NA = 1.45 100× air objective lens (Nikon) was used. The emitted light was recollected through the same objective, passed through 850-nm short-pass (Thorlabs, FESH 850) and 750-nm long-pass (Thorlabs, FELH 750) filters, and directed to a grating spectrometer (Ocean optics, QEPro) or a single-photon avalanche diode (Excelitas, SPCM-AQRH). A neutral density wheel, adjusted by an Arduino-controlled servo motor for varying optical densities, was used for power dependence measurements. These measurements were synchronized with the light collection system. Approximately 5% of the incoming light was directed to a Thorlabs power meter for simultaneous power recording. For time-resolved photoluminescence, the laser was modulated at 5 Hz using a function generator (National Instruments, CompactRIO), and emitted light was detected by the single-photon avalanche diode (SAPD). The photon-induced voltage pulses were counted by an FPGA board built into the CompactRIO system.

Photon avalanche-mediated confocal imaging simulation

The simulation began by setting the position of nanoparticles based on the relative coordinates from experimentally obtained optical images, ensuring a correlation with experimental results. Photon avalanche upconversion nanoparticles were modeled as 27 nm diameter disks, with 200 points within each disk to represent Tm^{3+} emitter dispersion. A scanning area of 300 nm by 300 nm was established, with 10,000 random points generated to determine laser beam positions for luminescence intensity collection.

The luminescence intensity for any given scanning point was calculated by integrating photons

emitted from ions within the nanoparticles as covered by the laser beam, using a numerical aperture of 1.45 and a 1064-nm Gaussian laser beam for the calculations. By methodically shifting the laser beam point-by-point and collecting intensity data, both photon avalanche upconversion intensity mapping and super-resolution imaging can be achieved. Critical for accurate simulations, the exact nanoparticle response to varying pumping intensities was determined because the Gaussian beam's intensity profile triggers photon avalanching across a range of intensities. The overall emission curve, as obtained experimentally, indicates the collective rather than the precise photon avalanche response. To isolate the actual photon avalanche response, a piecewise function was predefined. A universal global optimization algorithm (1stOpt 10.0, 7d-soft Pte Ltd) was then applied to fit the experimentally obtained power-dependent curve, allowing for the regression of the function's parameters.

Photon localization accuracy analysis

According to the theory of photon localization[7,8], calculating the accuracy of photon localization allows individual luminescent nanoparticles to be localized and tracked using optical microscopy. The two-dimensional localization precision can be written as:

$$\sigma_{xy} = \sqrt{\frac{s^2 + a^2/12}{N} + \frac{8\pi s^4 b^2}{a^2 N^2}}$$

where $\sigma_{x,y}$ is the localization precision of a luminescent nanoparticle in the lateral dimensions, s is the standard deviation of the point-spread function, N is the total number of photons collected from the nanoparticle, a denotes the pixel size in the image space, and b is the average background noise.

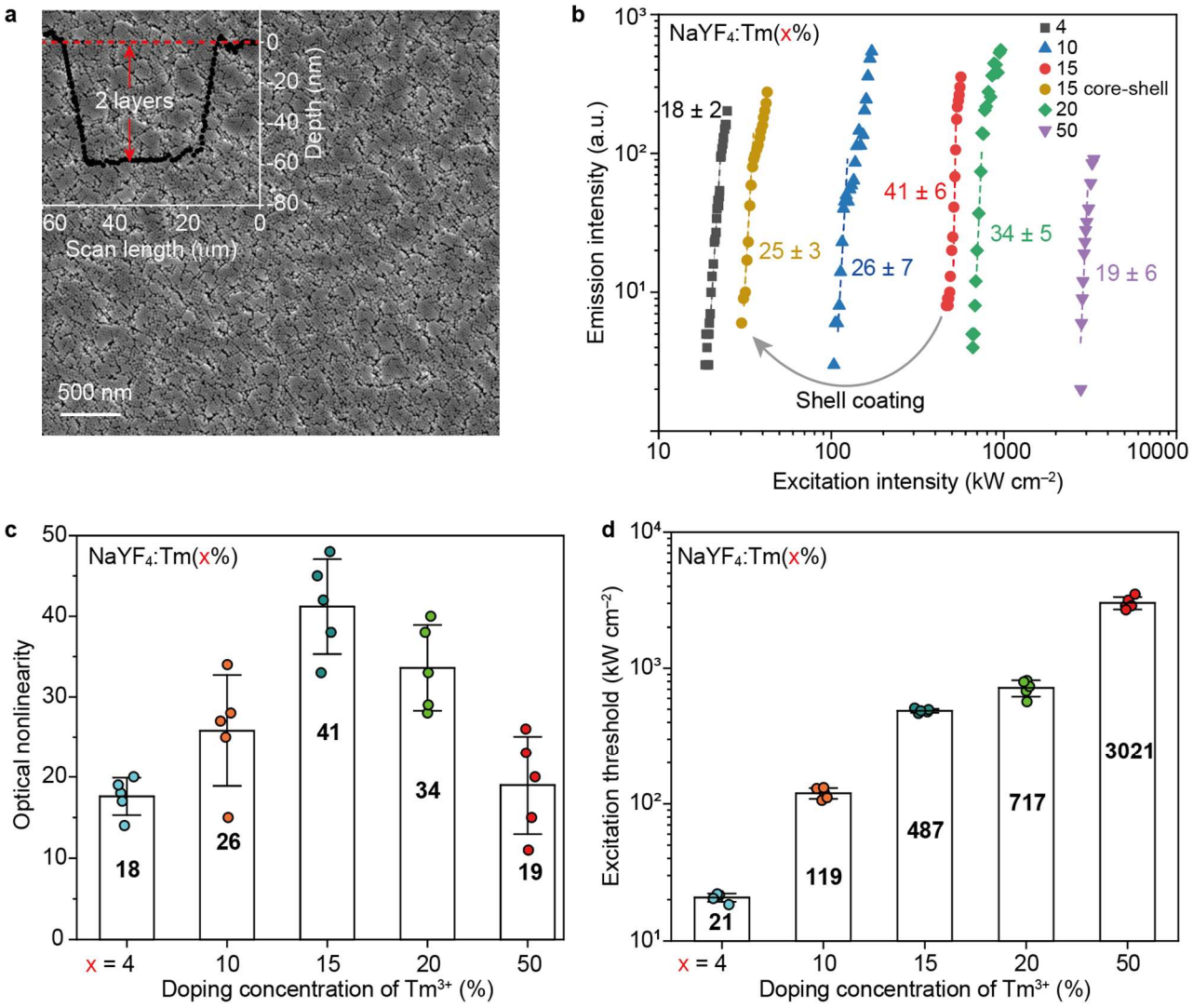

Supplementary Fig. 1 | **a,** Scanning electron microscopy (SEM) image showing a uniform film prepared for photon avalanching studies, with an inset illustrating the thickness profile of the film, approximately equivalent to two layers of nanocrystals. **b,** Graph depicting the power-dependent luminescence of Tm^{3+}-activated $NaYF_4$ nanocrystals with different Tm^{3+} doping concentrations, highlighting the effect of inert shell passivation on reducing optical nonlinearity. **c** and **d,** Graphs showing the statistical mean value of optical nonlinearity across samples (**c**) and the excitation thresholds (**d**) for initiating photon avalanche in $NaYF_4$:Tm nanocrystals.

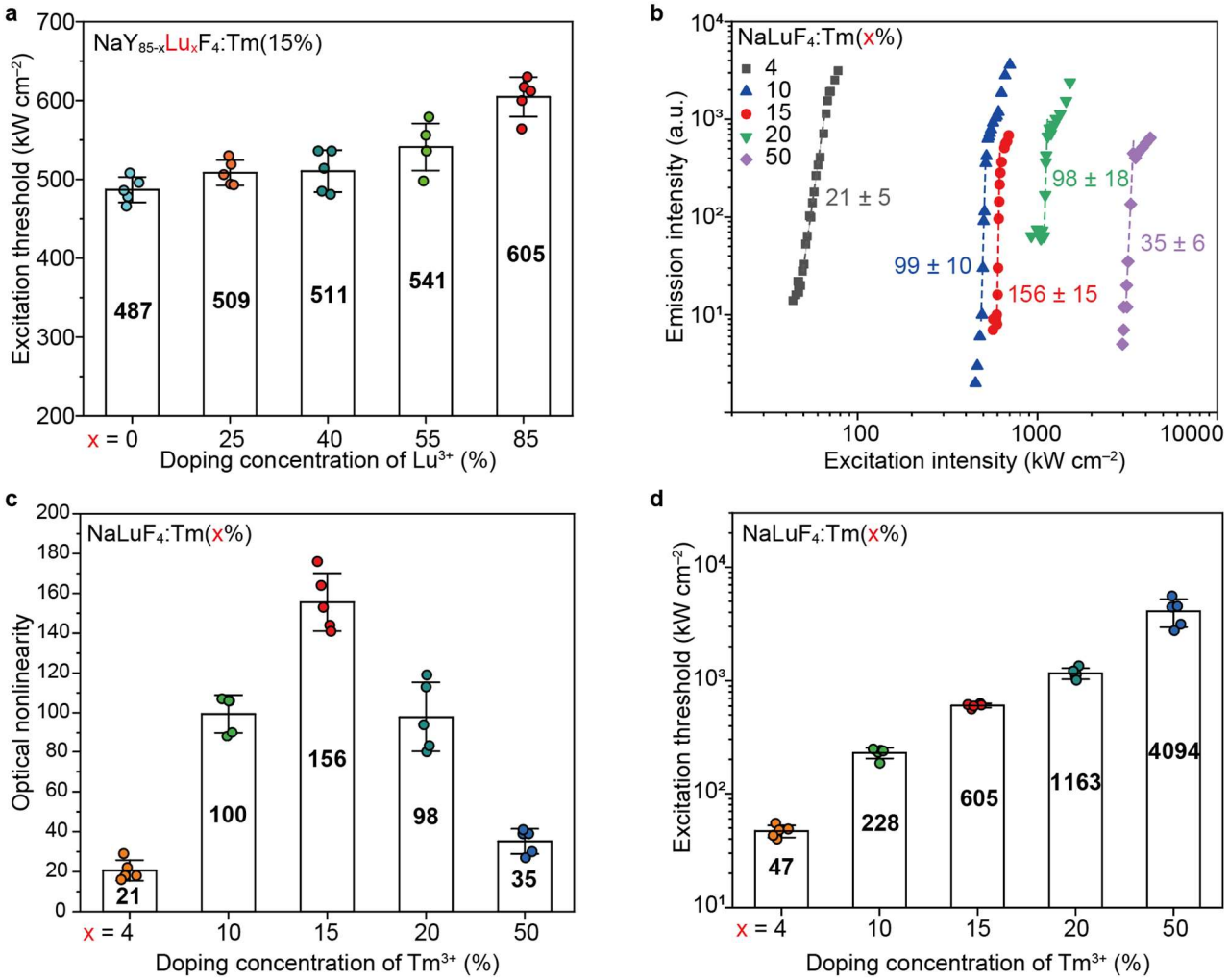

Supplementary Fig. 2 | **a,** Variation in optical nonlinearity among $NaYF_4$:Tm(15%) nanocrystals with different levels of Lu^{3+} substitution. **b,** Relationship between luminescence power-dependence and Tm^{3+}-doping concentration in Tm^{3+}-activated $NaLuF_4$ nanocrystals, indicating photon avalanching behavior. **c** and **d,** Graphs showing statistical data on optical nonlinearity (**c**) and excitation thresholds (**d**) for photon avalanche luminescence in $NaLuF_4$:Tm(x%) nanocrystals.

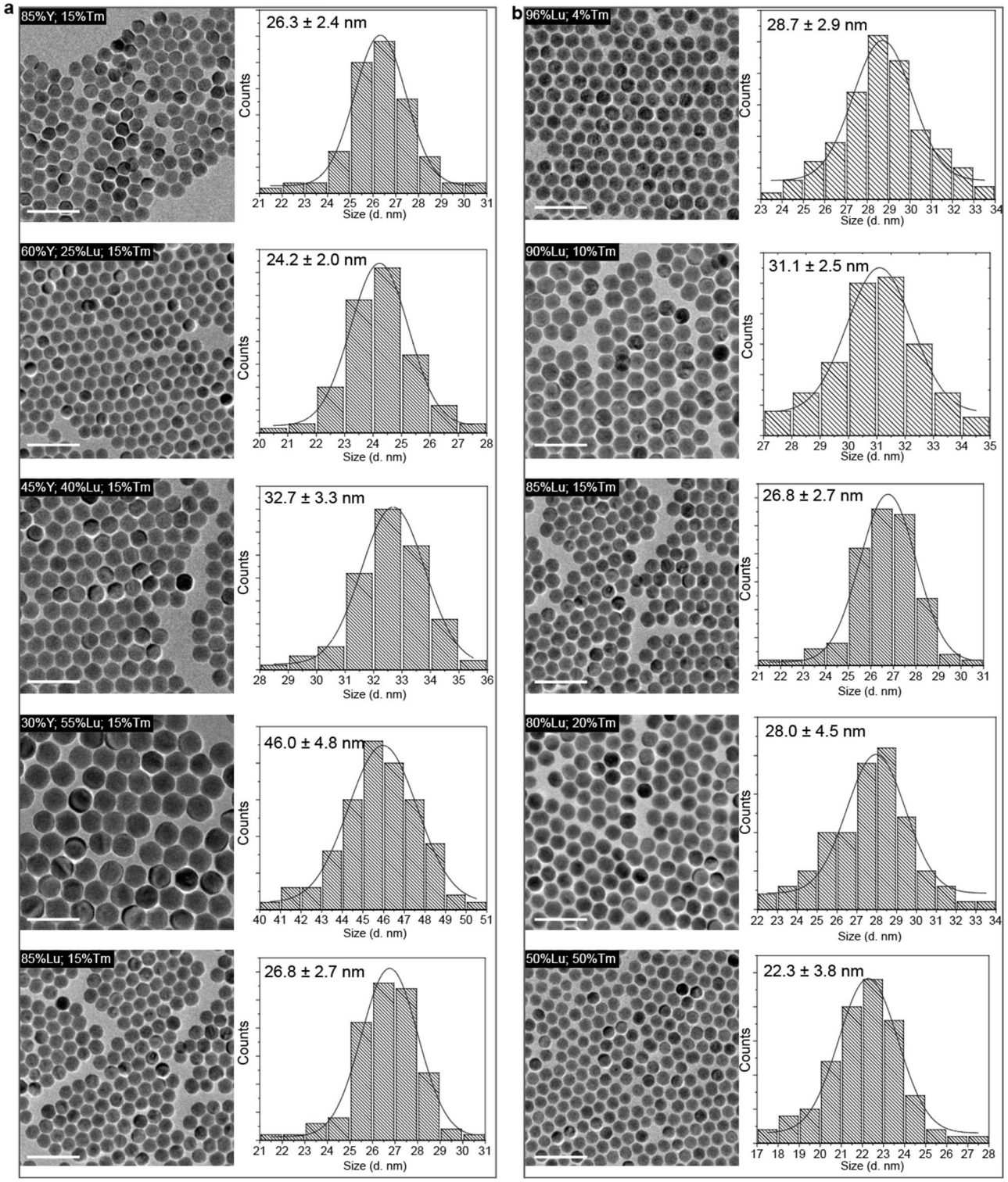

Supplementary Fig. 3 | **a,** Transmission electron microscopy (TEM) images of $NaYF_4$:Tm(15%) nanocrystals with different levels of Lu^{3+} substitution. **b,** TEM images of $NaLuF_4$:Tm nanocrystals at varying Tm^{3+} concentrations, accompanied by statistical size distribution charts for the prepared nanocrystals. Scale bar, 100 nm.

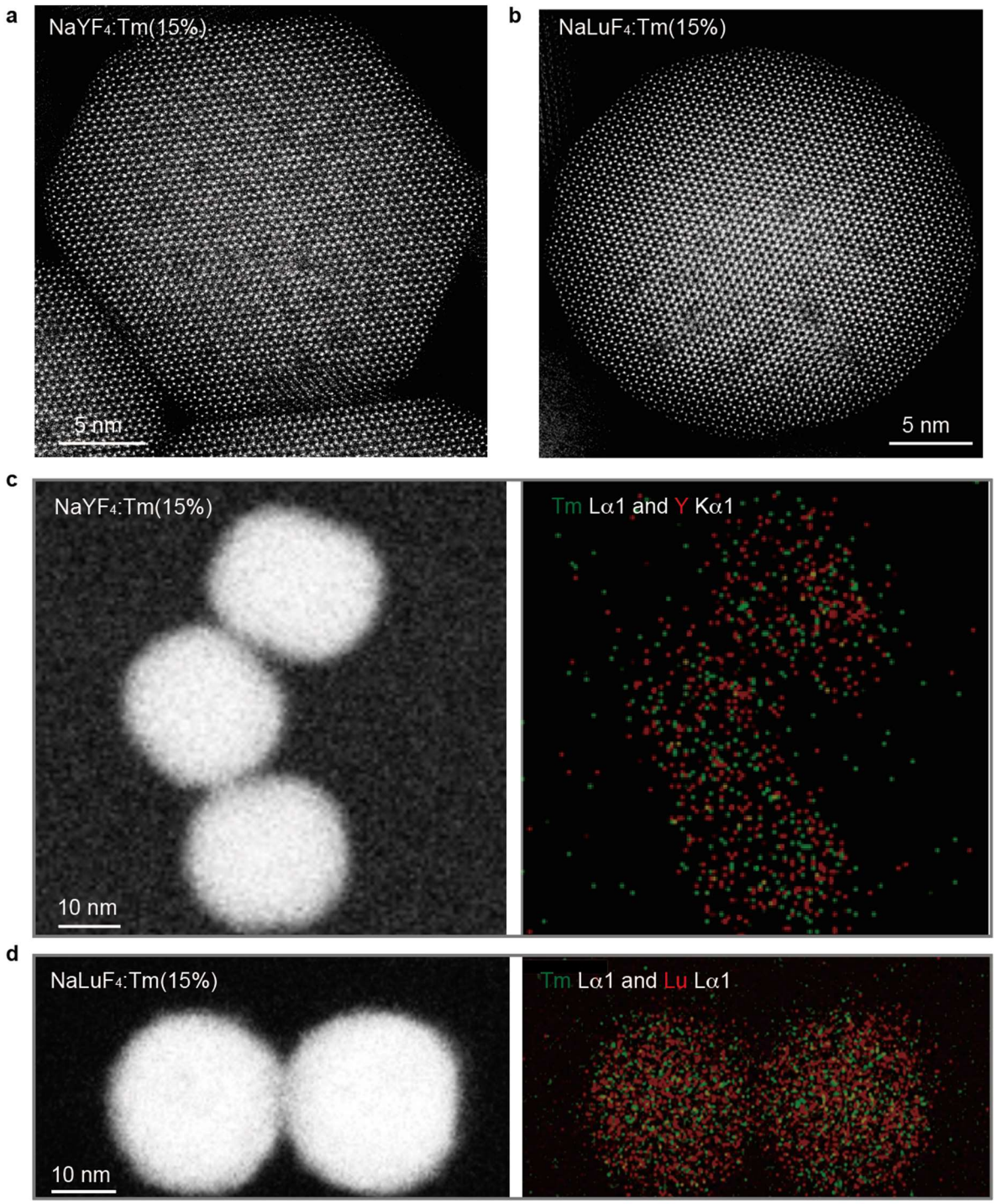

Supplementary Fig. 4 | **a** and **b,** High-resolution high-angle annular dark-field (HAADF) images showing the structural details of $NaYF_4$:Tm(15%) (**a**) and $NaLuF_4$:Tm(15%) (**b**) nanocrystals. **c** and **d**, Energy dispersive spectroscopy (EDS) mappings for $NaYF_4$:Tm(15%) (**c**) and $NaLuF_4$:Tm(15%) (**d**) nanocrystals.

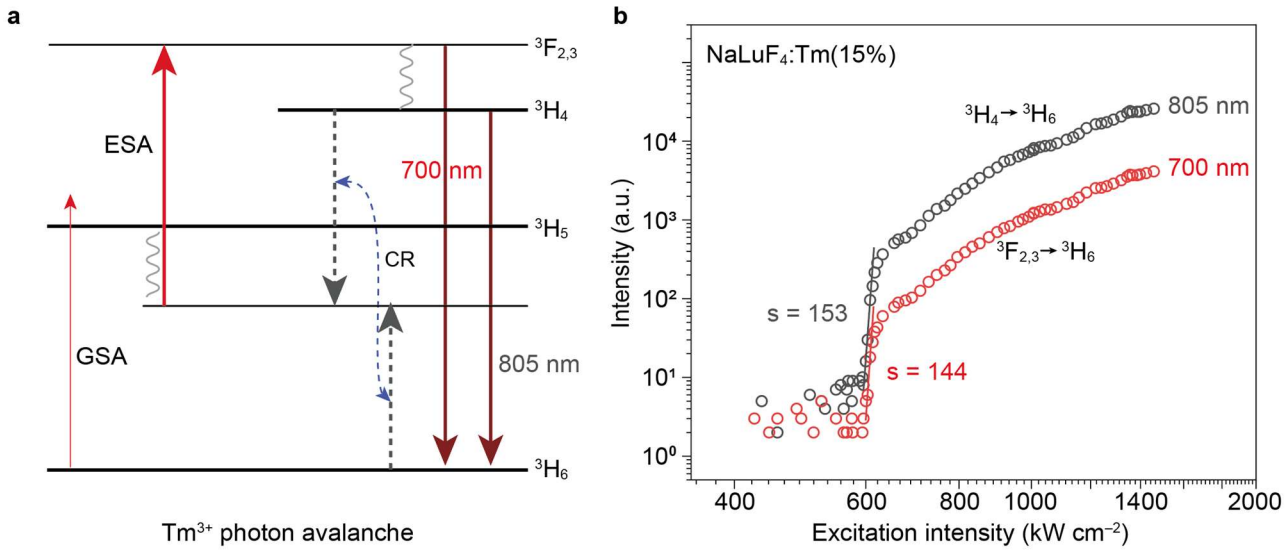

Supplementary Fig. 5 | **a,** Schematic illustrating the optical transitions that drive photon avalanche upconversion in Tm^{3+}-activated nanocrystals. **b,** Graph depicting the power-dependence for primary photon avalanching transitions in Tm^{3+}-activated nanocrystals, highlighting the relationship between excitation intensity and luminescence intensity.

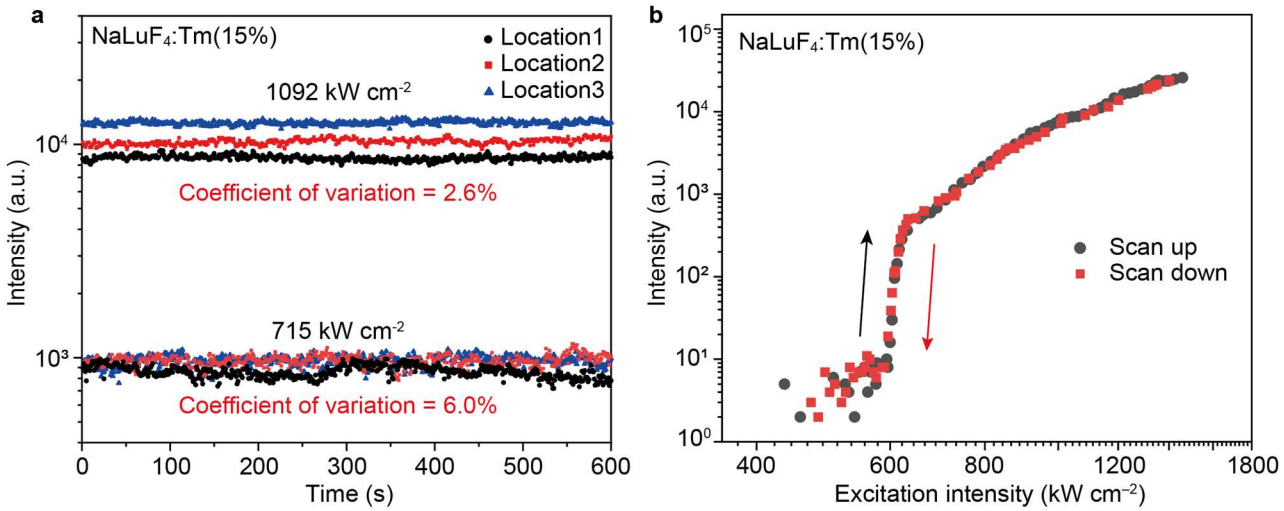

Supplementary Fig. 6 | **a,** Long-term photostability of $NaLuF_4$:Tm(15%) nanocrystals upon two different excitation intensities at three different locations. **b,** Bidirectional scanning imaging results showing the photon avalanching luminescence characteristics of $NaLuF_4$:Tm(15%) nanocrystals. This reveals the luminescence intensity's uniformity and intensity across different scanning directions.

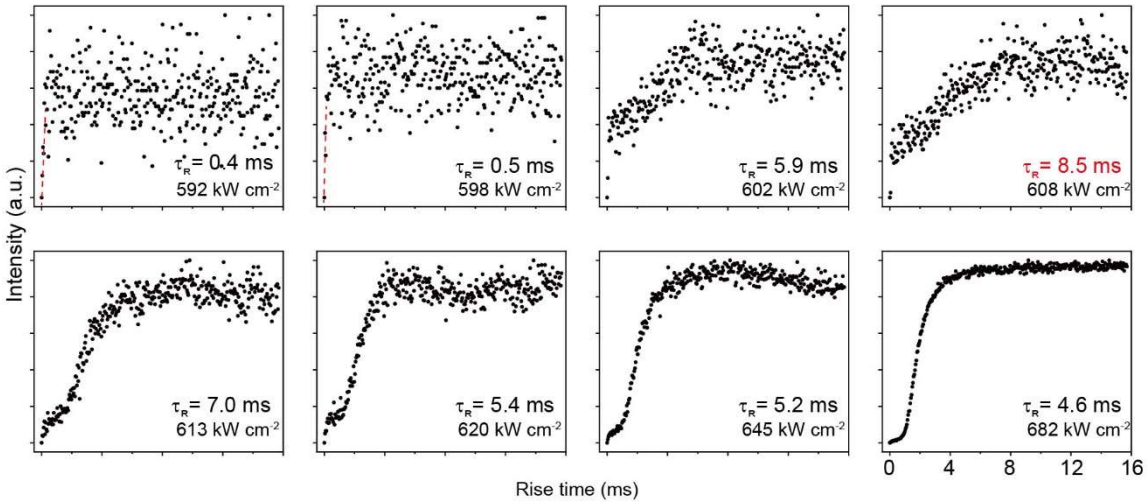

Supplementary Fig. 7 | Graphs and analyses exploring photon avalanching dynamics in $NaLuF_4$:Tm(15%) nanocrystals under a range of excitation intensities. The emphasis is on quantifying the dynamic rising time, which is defined as the duration it takes for the luminescence to reach 95% of its maximum steady-state intensity time, providing insights into the responsiveness of the nanocrystals to external excitation.

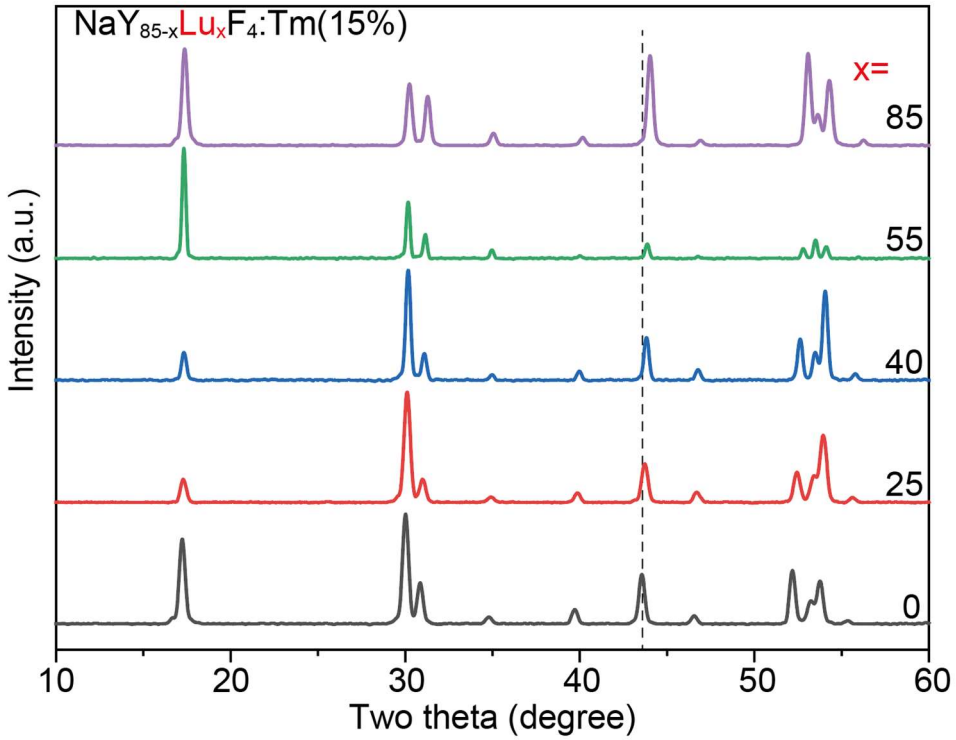

Supplementary Fig. 8 | X-ray diffraction patterns of $NaYF_4$:Tm(15%) nanocrystals with varying degrees of Lu^{3+} substitution. These patterns highlight structural changes resulting from different levels of substitution, affecting the crystalline structure.

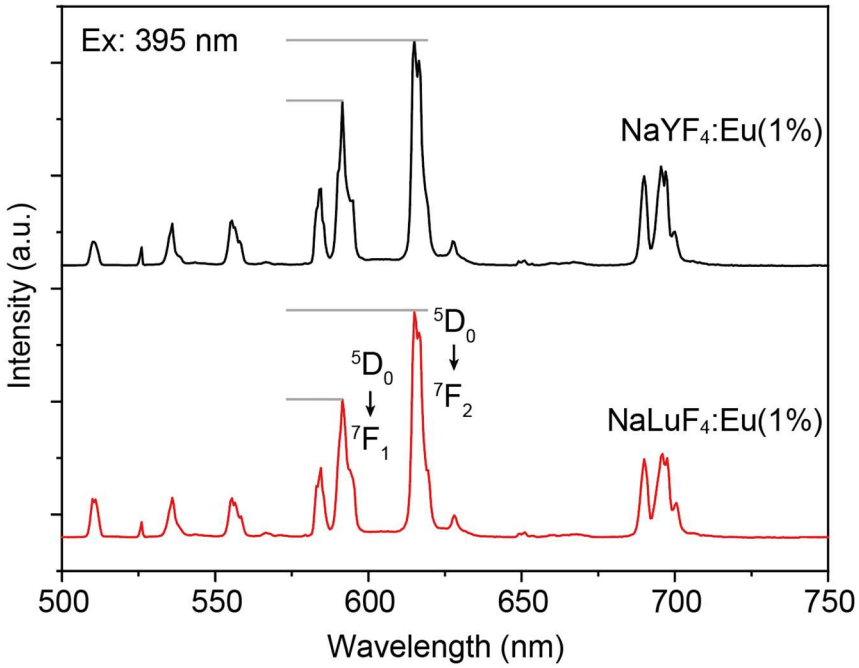

Supplementary Fig. 9 | Comparative emission spectra revealing the luminescent behavior of Eu^{3+}-activated $NaYF_4$ and $NaLuF_4$ nanocrystals upon excitation at 395 nm.

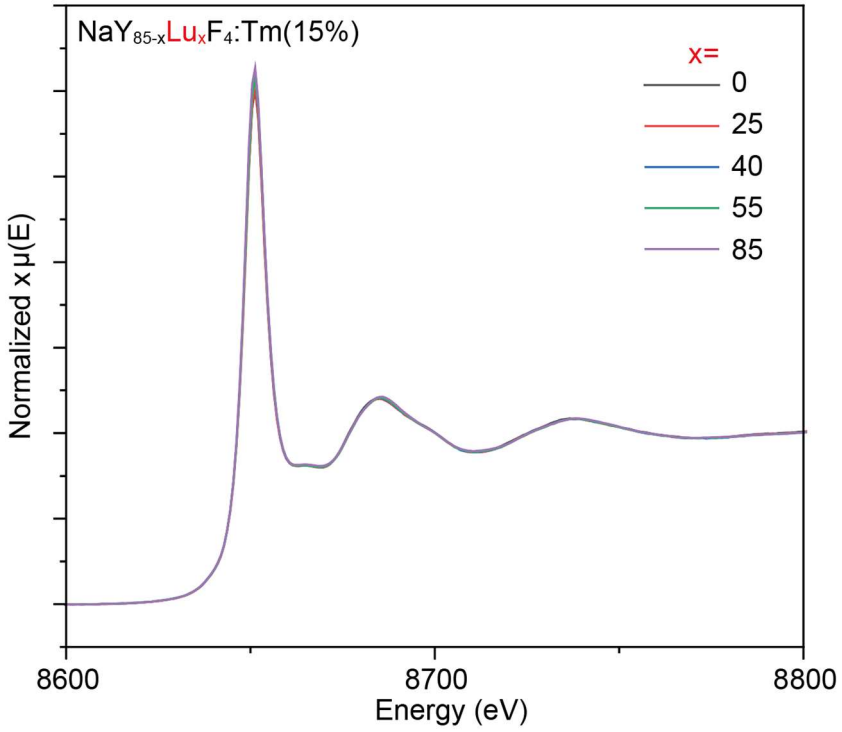

Supplementary Fig. 10 | Detailed analysis of the Tm-L_3 edge X-ray absorption near edge structure (XANES) for $NaY_{85-x}Lu_xF_4$:Tm(15%) nanocrystals, showing the effect of varying Lu substitution levels (x) on the electronic structure surrounding Tm ions.

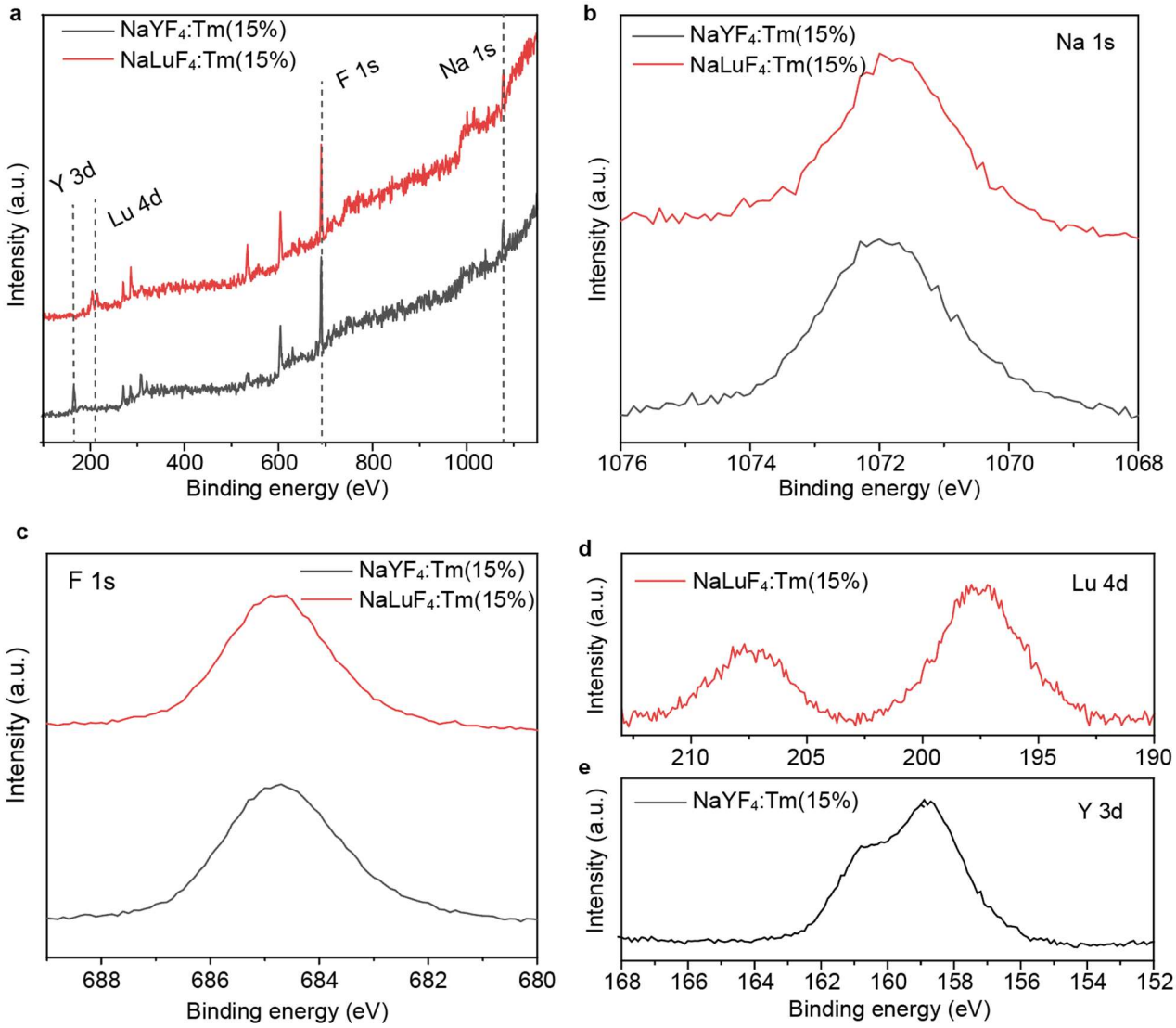

Supplementary Fig. 11 | **a,** Full-scan X-ray photoelectron spectra (XPS) of 27-nm $NaYF_4$:Tm(15%) and $NaLuF_4$:Tm(15%) nanocrystals. **b** and **c,** High-resolution XPS spectra of Na-1s (**b**) and F-1s (**c**) of $NaYF_4$:Tm(15%) and $NaLuF_4$:Tm(15%) nanocrystals, respectively. **d,** High-resolution XPS spectrum of Lu-4d for $NaLuF_4$:Tm(15%). **e,** High-resolution XPS spectrum of Y-3d for $NaYF_4$:Tm(15%).

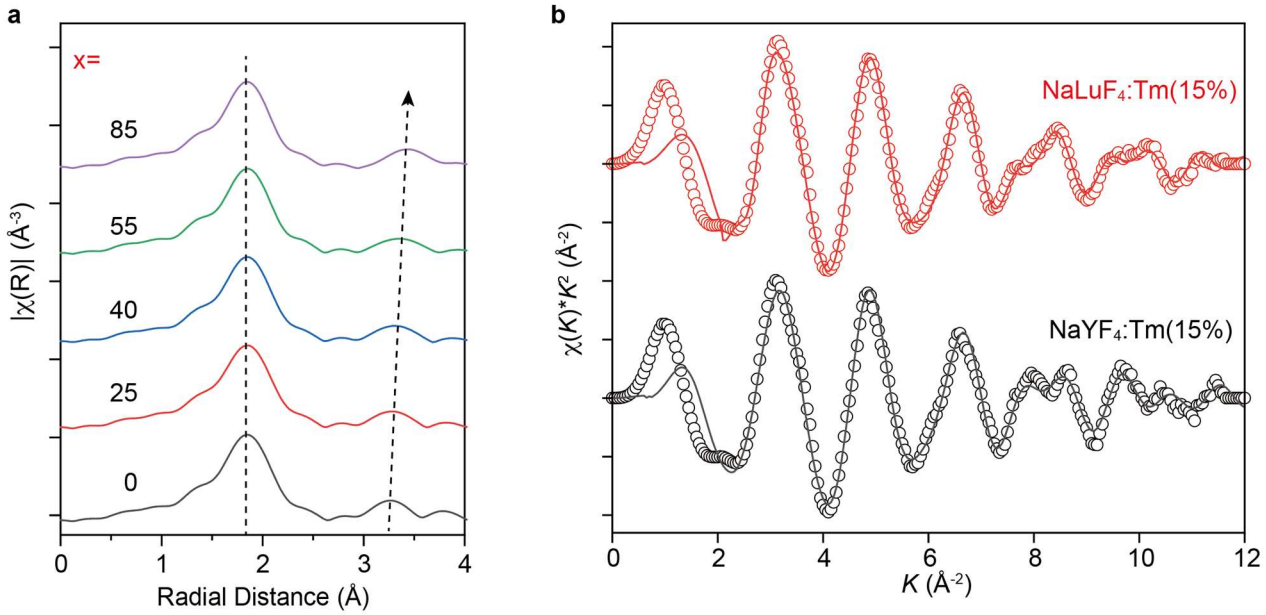

Supplementary Fig. 12 | **a,** Tm-L_3 edge EXAFS results in R-space. The data are k^2-weighted for clarity. **b**, Experimental (dots) and fitting (solid lines) results of Tm-L_3 edge EXAFS in k^2-weighted k-space.

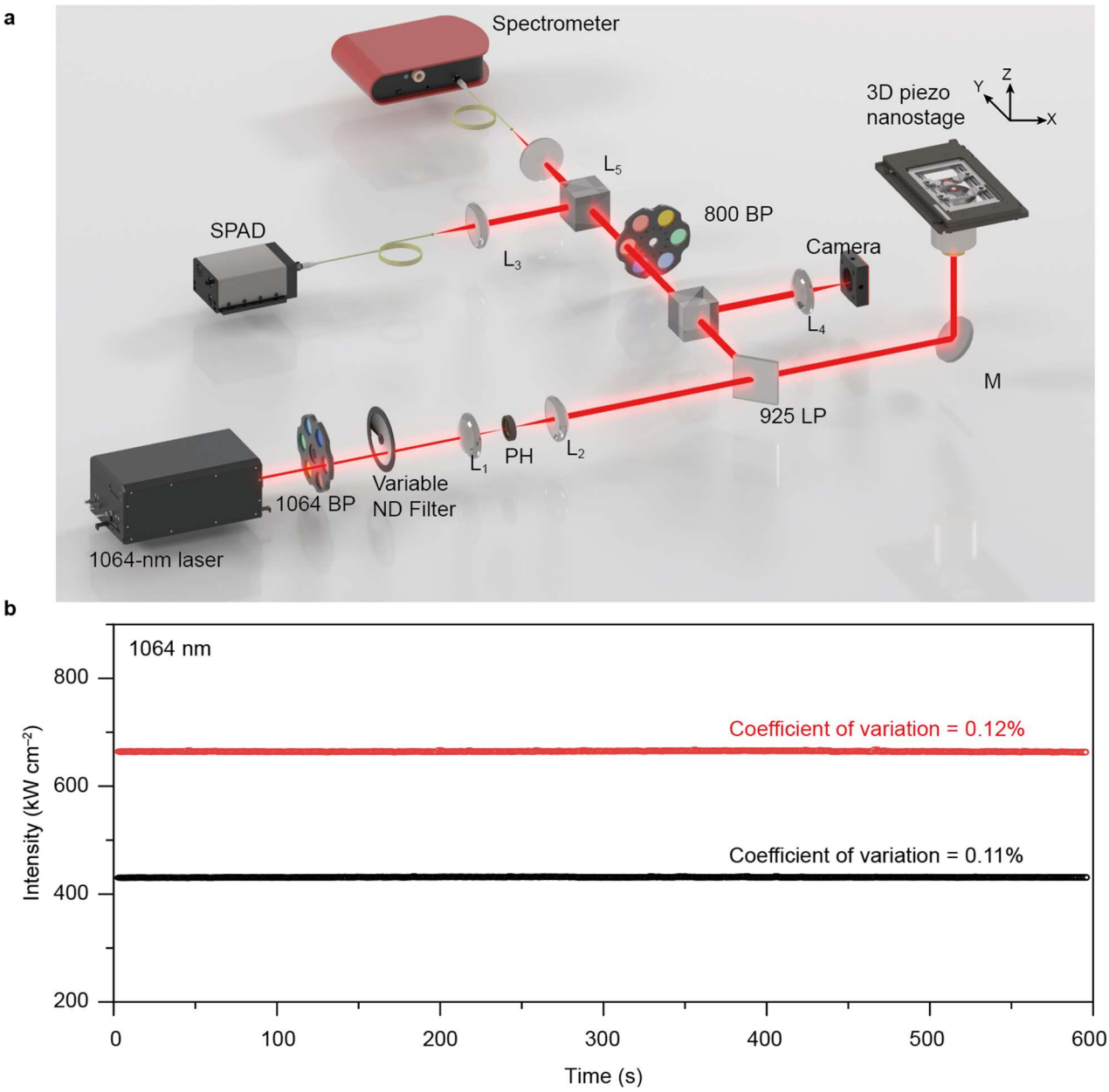

Supplementary Fig. 13 | a, Schematic of a custom-designed optical system for investigating photon avalanching luminescence, featuring lenses (L), mirrors (M), pinholes (PH), bandpass filters (BP), and a single-photon avalanche detector (SPAD). **b,** Results from a power stability test of a 1064 nm laser.

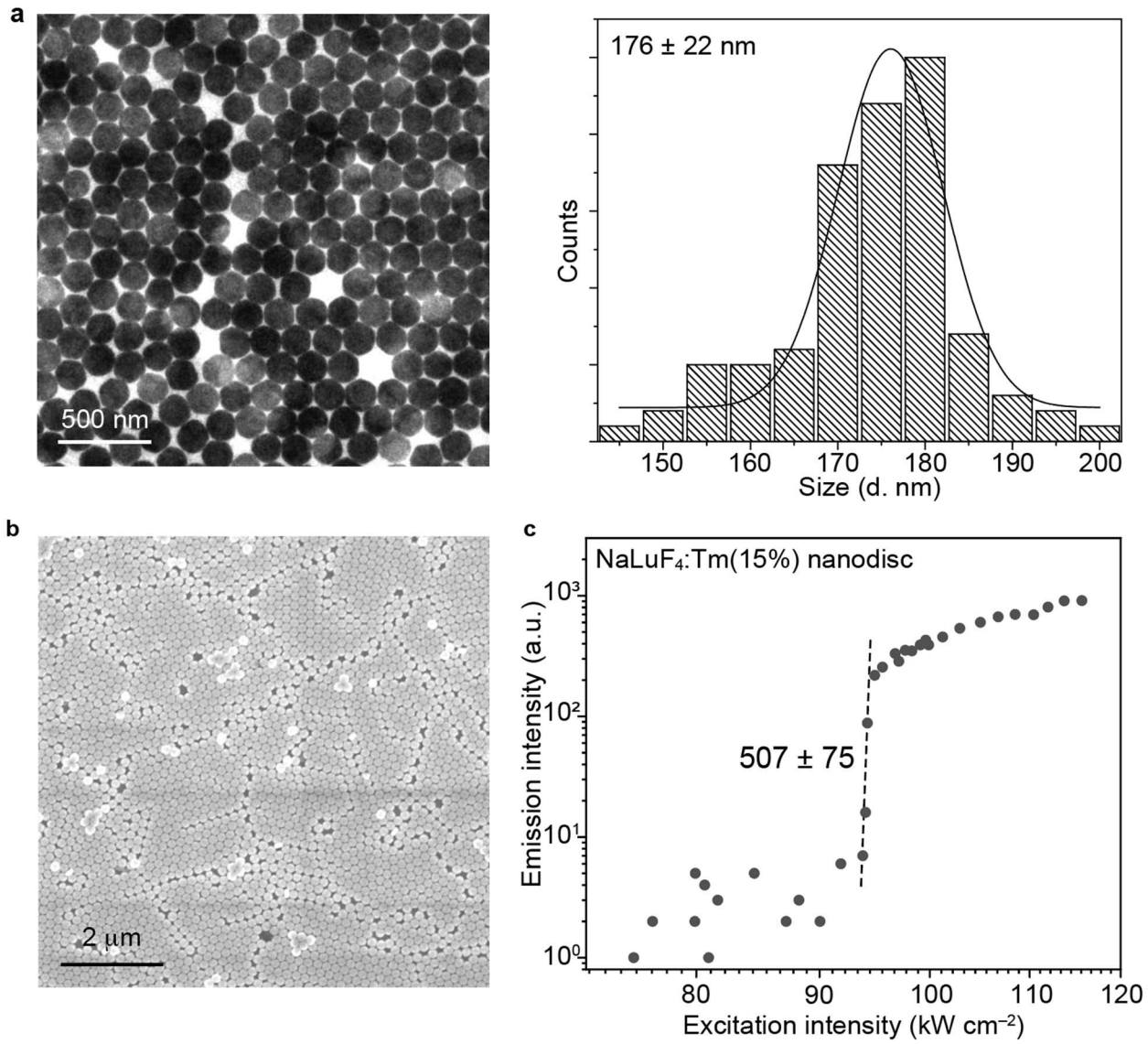

Supplementary Fig. 14 | **a-b,** TEM (**a**) and SEM (**b**) images of monolayer $NaLuF_4$:Tm(15%) nanodiscs, each with a diameter of approximately 176 nm. **c,** Measurement of photon avalanche optical nonlinearity exceeding 500, conducted on a monolayer film of $NaLuF_4$:Tm(15%) nanodiscs.

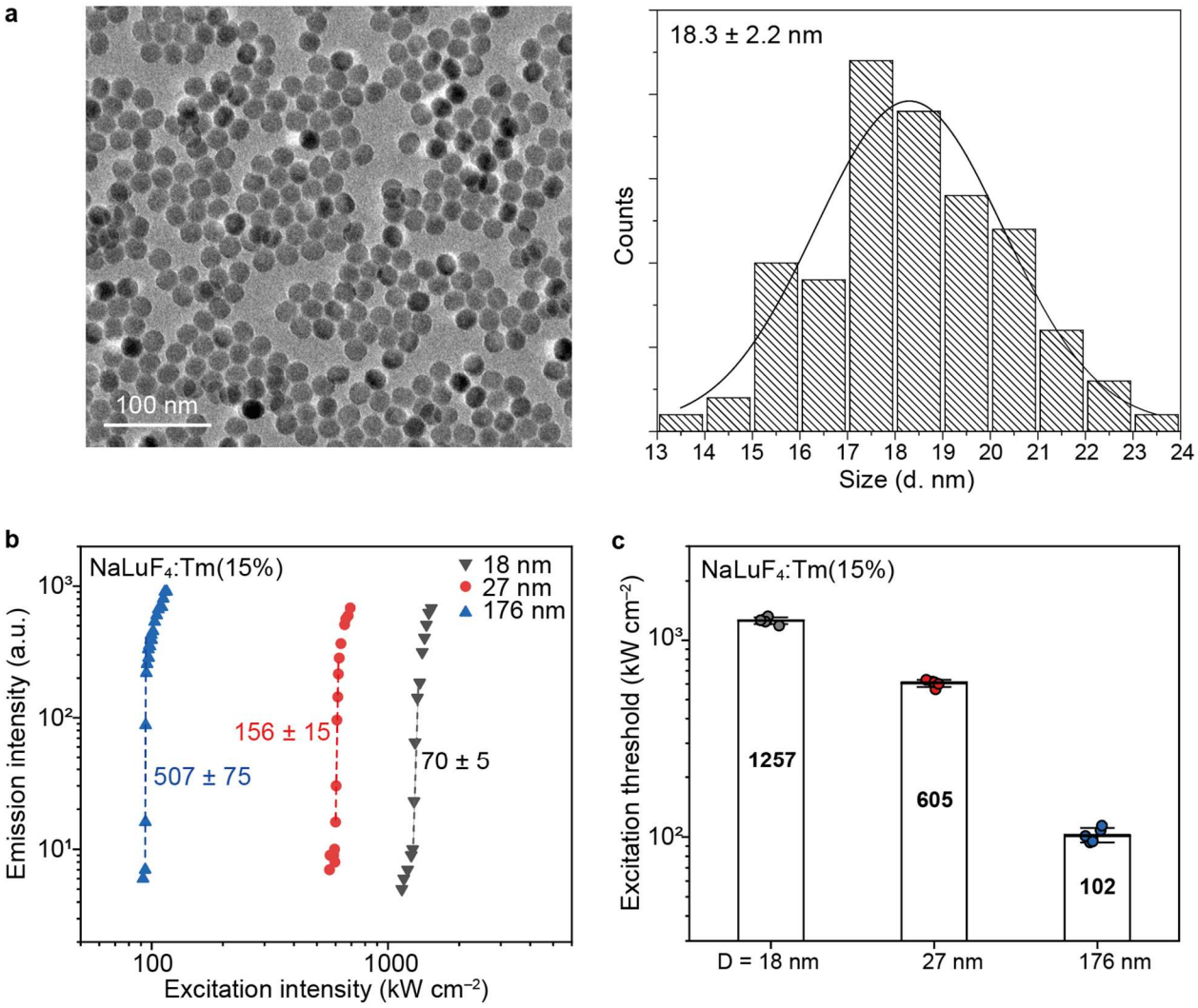

Supplementary Fig. 15 | **a,** TEM image and the corresponding size distribution graph for small-sized $NaLuF_4$:Tm(15%) nanoparticles (~18 nm in diameter). **b** and **c,** Analysis of photon avalanche nonlinearities (**b**) and their corresponding excitation thresholds (**c**) in $NaLuF_4$:Tm(15%) nanocrystals of varying diameters.

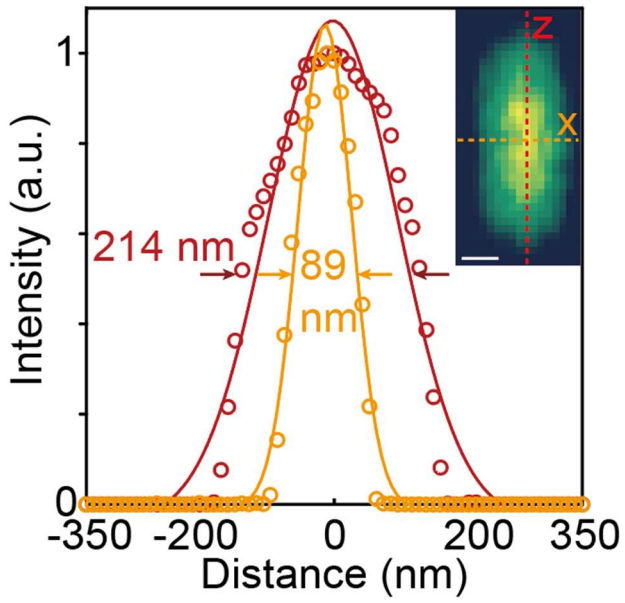

Supplementary Fig. 16 | Emission intensity profiles showing 3D photon avalanching super-resolution imaging of a $NaLuF_4$:Tm(15%) nanodisc, providing insights into the spatial distribution of luminescence at the nanoscale.

Supplementary Table 1 | Elemental compositions of various photon avalanching upconversion nanocrystals.

Nanocrystal	Actual molar ratio of Lu/Tm/Y
$NaLuF_4$:Tm(4%)	95.7/4.3/0
$NaLuF_4$:Tm(10%)	87.9/12.1/0
$NaLuF_4$:Tm(15%)	83.5/16.5/0
$NaLuF_4$: Tm(20%)	79.7/20.3/0
$NaLuF_4$: Tm(50%)	48.6/51.4/0
$NaY_{30}Lu_{55}F_4$:Tm(15%)	54.3/15.3/30.4
$NaY_{45}Lu_{40}F_4$:Tm(15%)	40.2/14.7/45.1
$NaY_{60}Lu_{25}F_4$:Tm(15%)	25.0/14.4/60.6
$NaYF_4$:Tm(15%)	0/14.7/85.3

Supplementary Table 2 | Comparison of the current work with previously reported achievements in photon avalanching technology, focusing on material innovation, nonlinearity, imaging resolution, and signal-to-noise ratio.

PA emitter	Host and dopant	D[a] (nm)	λ_{ex} [a] (nm)	λ_{em} [a] (nm)	I_{th} [a] (kW cm^{-2})	T_{rise} [a] (ms)	Nonlinearity	Resolution [b] (nm)	SNR[c]	Reference
Nd	KPb_2Cl_5:Nd (16%)	40	1064	810	10	70	11.9	-	-	Angew. Chem. Int. Ed. 62, e202212549 (2023)
Pr/ Yb	$NaYF_4$:Yb/Pr (15/0.5%) @$NaYF_4$	26	852	450-700	60	19.2	46	62	18.2	Nat. Nanotechnol. 17, 524–530 (2022)
Tm	$LiYF_4$:Tm (3%)@$LiYF_4$	30	1059	800	700	45	10.1	150	3.6	Adv. Opt. Mater. 10, 2201052 (2022)
Tm	$NaYF_4$:Yb/Tm (20/8%)	46	976	455	60		6.2	184	12.0	Nat. Commun. 10, 3695 (2019)
Tm	$NaYF_4$:Tm(8%) @$NaY_{80}Gd_{20}F_4$	28	1064	800	6	608	26	65	12.5	Nature 589, 230–235 (2021)
Tm	$KMgF_3$:Tm (5%)@$KMgF_3$	30	1064	802	16.6	281	27	-	-	Nano Lett. 23, 8576–8584 (2023)
Tm/Eu	$NaGdF_4$:Tm(20%)@ $NaGdF_4$@ $NaGdF_4$:Eu(15%)@$NaYF_4$	24	1064	800	16	87	15.1	-	-	Nano Lett. 23, 7100–7106 (2023)
Tm/Er	$NaYF_4$:Tm(8%)@$NaYF_4$:Er (5%)@$NaYF_4$:Er/Ce(5/5%)	46	1064	540	7.1	1100	41	-	-	Adv. Mater. 36, 2307848 (2024)
Tm	$NaLuF_4$:Tm(15%)	27	1064	805	605	8.5	156	33	43.1	This work
Tm	$NaLuF_4$:Tm(15%)	176	1064	805	102	-	507	89	1146	This work

[a]D, λ_{ex}, λ_{em}, I_{th}, and T_{rise} denote the diameter of nanocrystals, excitation wavelength, emission wavelength, the power density at photon avalanche threshold, and rising time, respectively. Dynamic rising time is determined as the time required to reach 95% of the steady-state emission intensity;

[b]Represents the Full Width at Half Maximum (FWHM);

[c]The signal-to-noise ratio (SNR) values were calculated as the ratio between the maximum intensity and the standard deviation of the background noise.

Supplementary movie 1 | Real-time automated data collection and analysis process of photon avalanche luminescence. This process involved testing a film composed of self-assembled monolayer nanoparticles to prove its exceptionally high optical nonlinearity and reliability.

Supplementary References

1 Wang, F. *et al.* Simultaneous phase and size control of upconversion nanocrystals through lanthanide doping. *Nature* **463**, 1061-1065 (2010).

2 Zhai, X. *et al.* Synthesis of small-sized hexagonal $NaREF_4$ (RE= Yb, Lu) nanocrystals through accelerating phase transformation. *J. Lumin.* **244**, 118694 (2022).

3 Dong, A., Chen, J., Vora, P. M., Kikkawa, J. M. & Murray, C. B. Binary nanocrystal superlattice membranes self-assembled at the liquid–air interface. *Nature* **466**, 474-477 (2010).

4 Ravel, B. & Newville, M. ATHENA, ARTEMIS, HEPHAESTUS: data analysis for X-ray absorption spectroscopy using IFEFFIT. *J. Synchrotron Radiat.* **12**, 537-541 (2005).

5 Du, Y. *et al.* XAFCA: a new XAFS beamline for catalysis research. *J. Synchrotron Radiat.* **22**, 839-843 (2015).

6 Newville, M. IFEFFIT: interactive XAFS analysis and FEFF fitting. *J. Synchrotron Radiat.* **8**, 322-324 (2001).

7 Thompson, R. E., Larson, D. R. & Webb, W. W. Precise nanometer localization analysis for individual fluorescent probes. *Biophys. J.* **82**, 2775-2783 (2002).

8 Thompson, M. A., Lew, M. D. & Moerner, W. Extending microscopic resolution with single-molecule imaging and active control. *Annu. Rev. Biophys.* **41**, 321-342 (2012).